Retrieval of Gridded Aerosol Direct Radiative Forcing Based on Multiplatform Datasets

Yanyu Wang[1], Rui Lyu[1], Xin Xie[1], Ze Meng[2], Meijin Huang[3], Junshi Wu[4], Haizhen Mu[4], Qiu-Run Yu[5], Qianshan He[4,6*], Tiantao Cheng[,7,8,1*]

[1]Shanghai Key Laboratory of Atmospheric Particle Pollution and Prevention (LAP[3]), Department of Environmental Science and Engineering, Institute of Atmospheric Sciences, Fudan University, Shanghai, 200438, China

[2]School of Oceanography, Shanghai Jiao Tong University, Shanghai, 200030, China

[3]Fujian Meteorological Observatory, Fuzhou, 350001, China

[4]Shanghai Meteorological Service, Shanghai, 200030, China

[5]Key Laboratory of Meteorological Disaster, Ministry of Education (KLME)/Joint International Research Laboratory of Climate and Environment Change (ILCEC), Nanjing University of Information Science and Technology, Nanjing, 210044, China

[6]Shanghai Key Laboratory of Meteorology and Health, Shanghai, 200030, China

[7]Department of Atmospheric and Oceanic Sciences, Institute of Atmospheric Sciences, Fudan University, Shanghai, 200438, China

[8]Shanghai Institute of Eco-Chongming (SIEC), Shanghai, 200062, China

Correspondence to: Qianshan He (oxeye75@163.com); Tiantao Cheng (ttcheng@fudan.edu.cn).

Abstract. Atmospheric aerosols play a crucial role in regional radiative budgets. Previous studies on clear-sky aerosol direct radiative forcing (ADRF) have mainly been limited to site-scale observations or model simulations for short-term cases, and long-term distributions of ADRF in China has not been portrayed yet. In this study, an accurate fine-resolution ADRF estimate at the surface was proposed. Multiplatform datasets, including satellite (MODIS aboard Terra and Aqua) and reanalysis datasets, served as inputs to the Santa Barbara Discrete Atmospheric Radiative Transfer (SBDART) model for ADRF simulation with consideration of aerosol vertical profile over East China during 2000-2016. Specifically, single scattering albedo (SSA) from the Modern-Era Retrospective Analysis for Research and Application, version 2 (MERRA-2) was validated with sunphotometers over East China. The gridded asymmetry parameter (ASY) was then simulated by matching the calculated top-of-atmosphere (TOA) radiative fluxes from the radiative transfer model with satellite observations (Clouds and the Earth's Radiant Energy System (CERES)). The high correlation and small discrepancy (6-8 W m^{-2}) between simulated and observed radiative fluxes at three sites (Baoshan, Fuzhou, and Yong'an) indicated that ADRF retrieval is feasible and has high accuracy over East China. Then this method was applied in each grid of East China, and the overall picture of ADRF distributions over East China during 2000-2016 was displayed. ADRF ranges from -220 to -20 W m^{-2}, and annual mean ADRF is -100.21 W m^{-2}, implying that aerosols have strong cooling effect at the surface in East China. With the economic development and rapid urbanization, the spatiotemporal changes of ADRF during past 17 years are mainly attributed to the changes of anthropogenic emissions in East China. Our method provides the long-term ADRF distribution over East China for the first time, highlighting the importance of aerosol radiative impact under climate change.

1 Introduction

Atmospheric aerosols play a significant role in air quality, regional/global climate and human health (Wang et al., 2018; Wang et al., 2019). Aerosols can directly absorb and scatter solar radiation, and indirectly affect cloud formation and precipitation by acting as cloud condensation nuclei or ice nuclei (Twomey, 1977; Rosenfeld, 1999). Large amounts of scattering aerosols can generally attenuate incoming solar radiation. This reduction in surface radiation significantly impacts the surface
40 temperature, crop growth and solar energy availability (Chameides, 1999; Liao et al., 2015). On the other hand, highly absorbing aerosols, such as black carbon, can warm the atmosphere, alter regional atmospheric stability, and even influence the large-scale circulation and hydrologic cycle with significant regional climate effects (Menon et al., 2002; Wang, J. et al., 2009). Aerosol direct radiative forcing (ADRF) is a good metric for evaluating the impact of aerosols to radiation by absorption and scattering, and is defined as the difference between the net radiative flux of earth-atmosphere systems with and without
45 aerosols. Anthropogenic aerosols produce a global mean negative direct radiative forcing of -0.35±0.5 W m^{-2} of ADRF, which has dampened the warming effect of greenhouse gases (IPCC, 2013). However, the current assessment of ADRF remains highly uncertain. This uncertainty mainly results from the large variations in aerosol concentrations, chemical compositions, optical properties, mixing states, and vertical profiles (Haywood and Boucher, 2000; Tian et al., 2018a). Therefore, an accurate and feasible method for ADRF retrieval is greatly required.

50 Reduction in these uncertainties requires the integration of different techniques and datasets (e.g., surface measurement, model simulation, and satellite remote sensing) (Yu et al., 2006). To better understand aerosol optical properties and their radiative effect, several ground-based networks have been established worldwide, such as the AEROsol Robotic Network (AERONET) (Holben et al., 2001), Global Atmosphere Watch-Precision Filter Radiometer network (GAW-PFR) (Nyeki et al., 2015), China Aerosol Remote Sensing Network (CARSNET) (Che et al., 2009) and Chinese Sun Hazemeter Network (CSHNET) (Xin et
55 al., 2007). Moreover, intensive field experiments have been carried out over China, such as Beijing, Xianghe, Taihu, Wuhan, Shanghai, Lanzhou (Li et al., 2003; He et al., 2012a; Wang et al., 2014; Yu et al.,2016a; Gong et al., 2017; Zhang et al.,2018). Such measurements are conducive to the wider knowledge of aerosol properties, which are helpful for improving the performance of satellite and model simulations through synthesis. Nevertheless, available measurements are usually restricted in terms of spatial and temporal coverage. In addition to surface measurements, model simulations play an indispensable role
60 in the estimation of the aerosol radiative effect at the global scale and excel in predicting past or future trends of ADRF (Chang and Liao, 2009; Qiu et al., 2017). Meanwhile, model simulations are subject to large uncertainties in terms of emissions, transport, and physical and chemical parametrization schemes (José A. et al., 2013).

Compared to the above methods, satellite remote sensing has an outstanding advantage of delivering aerosol information with higher spatial resolution and larger spatial coverage. Using solely satellite data or a combination with model simulations and
65 observations constraint, many methods have been developed to retrieve global and regional ADRF estimates (e.g., Yu et al., 2004; Bellouin et al., 2005; De Graaf et al., 2013). However, these studies have mainly concentrated on the top-of-atmosphere (TOA) radiation budget. Thus far, long-term estimates of the surface ADRF distribution have rarely been addressed and few

studies gave a full picture of surface ADRF over land (e.g.: Thomas et al., 2013; Chung et al., 2016). This lack of research is because satellites are unable to measure surface-level radiative fluxes directly. Furthermore, the retrieval of aerosol microphysical parameters remains challenging, including single scattering albedo (SSA, see Table 1 for the acronyms) and asymmetry parameter (ASY). Many attempts have been made to solve this key problem. For instance, Thomas et al. (2013) adopted prescribed aerosol properties from the literature to estimate surface ADRF. Fu et al. (2017) took aerosol optical parameters from some AERONET sites as representative of the entire region to conduct grid-cell ADRF simulations. Undoubtedly, additional uncertainty was introduced by the assumption of aerosol optical representativeness in the temporal and spatial dimensions. Some studies also nudged global model simulations towards AERONET SSA to obtain the aerosol parameters (Chung et al., 2016). With the rapid development of satellite technology, more satellites are providing more detailed aerosol optical products via instruments such as the Polarization and Directionality of the Earth's Reflectance instrument (POLDER), and the Ozone Monitoring Instrument (OMI) (Levelt, et al., 2006; Tilstra and Stammes, et al., 2007). However, the accuracy of the SSA and ASY products over China still needs to be improved (Oikawa et al., 2013; Dubovik, et al., 2019). Recently, using satellite and observational data assimilated into the Goddard Earth Observing System, version 5 (GEOS-5), the National Aeronautics and Space Administration (NASA) has extended the Modern-Era Retrospective Analysis for Research and Application, version 2 (MERRA-2). Compared with its predecessor (MERRA-1), MERRA-2 offers important improvements in aerosol assimilations (Gelaro et al., 2017). The new dataset has the potential to provide improved estimates of aerosol microphysical parameters, such as SSA, and can be further used in the ADRF estimation. After SSA is determined, ASY, the only unknow model input, can be retrieved by matching the simulated radiative fluxes with satellite measurements from Clouds and the Earth's Radiant Energy System (CERES). Overall, based on the satellite and reanalysis datasets, including MERRA-2, the MODerate Resolution Imaging Spectroradiometer (MODIS) and CERES, the objective of this study is to provide quantitative estimates of fine-resolution ADRF distributions under the clear skies using a radiative transfer model over East China (114°-124°E, 24°-38°N, shown in the Figure 1). Additionally, the aerosol vertical profiles in each grid, which were not considered in previous studies, are used to obtain more accurate ADRF. In our study, aerosol vertical profiles are determined by the Weather Research and Forecasting Model (WRF, version 3.2.1) and the National Centers for Environmental Prediction-Final Operational Global Analysis (NCEP-FNL). The detailed algorithm of aerosol profiles can be found in Section 2. Other data acquisition is also presented in Section 2, and Section 3 introduces the method of ADRF simulations. Section 4 includes the retrieval of aerosol optical properties, validation of surface radiative fluxes with pyranometers, and detailed discussion of the error sources. Then this method is applied in each grid of East China during 2000-2016, and the uncertainty in the retrieval method is also discussed in Section 4. The conclusion is presented in Section 5.

2 Data

To acquire ADRF, the inputs (aerosol optical depth (AOD), SSA, ASY, albedo, etc.) to the radiative transfer model were determined from a combination of satellite and reanalysis datasets. AOD was derived from Collection 6 (C6) of MODIS Level 2 products over land (10-km resolution at the nadir) from the Terra satellite (Levy et al., 2013). Compared with C5, MODIS

3

C6 mainly updated the cloud mask to allow heavy smoke retrievals and fine-tuned the assignments for aerosol types as function of season and location over the land. Levy et al. (2013) made a comparison between MODIS C5, C6 and AERONET, and found that the correlation coefficient of C6/AERONET increases slightly, and the slope and offset of the regression curve only changed slightly compared with C5/AERONET. MODIS AOD retrieval primarily employs three spectral channels, centered

105   at 0.47, 0.66, and 2.1 μm and is interpolated at 0.55 μm (Kaufman et al., 1997). Li et al. (2003) demonstrated that the MODIS AOD Level 2 product is appropriate in eastern China and exhibits high precision. In addition, He et al. (2010) found that MODIS AOD was highly correlated with sunphotometer (CE318) measurements at 7 sites in the Yangtze River Delta (YRD) region (118°-123°E, 29°-33°N), with a correlation coefficient of 0.85 and with 90% of cases falling in the range of ΔAOD = $\pm$ 0.05 $\pm$ 0.20 AOD (Chu et al., 2002). Thus, the uncertainty in the AOD is regarded as 20% in this study.

110   Hourly SSA product was provided by MERRA-2. MERRA-2 combines GEOS-5 and the three-dimensional variational data assimilation (3DVar) Gridpoint Statistical Interpolation analysis system (GSI). GEOS-5 is coupled to the Goddard Chemistry, Aerosol, Radiation and Transport (GOCART) aerosol module, which includes five particulate species (sulfate, dust, sea salt, organic and black carbon) (Colarco et al., 2010). The optical properties of these aerosols are primarily from the Optical Properties of Aerosols and Clouds (OPAC) dataset, in which aerosol optical parameters are calculated based on the

115   microphysical data (size distribution and spectral refractive index) under the assumption of spherical particles and they are given for up to 61 wavelengths between 0.25 and 40 μm (Hess et al., 1998). MERRA-2 provides SSA data at 0.55 μm. It is calculated by the ratio of total aerosol scattering aerosol optical thickness (AOT) to total aerosol extinction AOT at 0.55 μm, and these two are the outputs of GOCART model (Colarco et al., 2010). More details of the aerosol module in MERRA-2 can be found in Randles et al. (2017) and Buchard et al. (2017). The new dataset has been used in many recent studies and is

120   appropriate for environmental and atmospheric research (Song et al., 2018). The input SSA was interpolated to other wavelength in SBDART, which will be discussed detailly in the Methodology (Section 3).

The upward radiative flux at TOA was used to constrain and determine the ASY. The shortwave (SW, 0.3-5 μm) TOA flux was acquired by CERES Single Scanner Footprint (SSF) level 2 product from Terra satellite. CERES SSF measures the instantaneous reflected SW radiance under clear-sky conditions. To convert from radiance to flux, angular distribution models

125   (ADM) were used in the CERES SSF product (Loeb et al., 2003). The CERES file contains one hour of data, and the CERES SSF footprint nadir resolution is approximately 20 km. According to Su et al. (2015), the uncertainty of TOA SW flux is 1.6% over clear land.

Another important parameter for ADRF simulations is the surface albedo, and it was derived from daily MODIS MCD43C3 black-sky albedo product (C6). Surface albedo product includes seven narrow bands and three broadbands (visible (0.3-0.7

130   μm), near-infrared (0.7-5.0 μm), and SW (0.3-5 μm)). Here, albedo product in SW band was used in our study. Each file contains 16 days of combined Level 3 data from the satellites Aqua and Terra, with a spatial resolution of 0.05°. It also contains the data quality information, that is, the proportion of inversion retrieval information in each pixel. For example, data quality index 0 represents the best quality (100% with full inversion and no fill values), this index increases with the decrease of the proportion of inversion retrieval pixel, and 4 represents 50% or less fill values. Notably, to ensure accuracy, only the albedo

135   values with high quality index (0-4) were used. The uncertainty in the high-quality MODIS albedo is less than 5% (Cescatti et al., 2012).

The total column ozone, total column water vapor and atmospheric profile data were from the ERA-Interim (European Center for Medium-Range Weather Forecast (ECMWF) Interim Reanalysis). Specifically, the atmospheric profile includes the altitude, temperature, water vapor density, and ozone density at 37 pressure levels (1, 2, 3, 5, 7, 10, 20, 30, 50, 70, 100 to 250

140   at 25-hPa intervals, 300 to 750 at 50-hPa intervals, and 775 to 1000 at 25-hPa intervals). The data quality of the ERA-Interim reanalysis data can be found in Dee et al. (2011).

The aerosol vertical profile plays a non-negligible role in aerosol radiative forcing. In SBDART, aerosol vertical profile is shaped by aerosol density and the according altitude. The aerosol density is a proportion of AOD in different altitude, and the overall profile is scaled by AOD. The aerosol density is set to fall exponentially between two altitudes by default. In our study,

145   aerosol vertical profile in SBDART was derived from two-layer aerosol vertical distribution model, which is proposed by He et al. (2008). In this two-layer aerosol model (Figure S1), aerosol extinction coefficient is assumed to decrease exponentially with altitude above the top of the planet boundary layer (PBL) and the extinction coefficient keeps uniform below the PBL. Based on this aerosol model, two inputs of aerosol vertical profile need to be determined, PBL and aerosol layer height (ALH). ALH is defined as the level where the aerosol extinction coefficient decreases to 1/e (scaling height) of that at the top of the

150   PBL. PBL and ALH input to SBDART along with the according aerosol density. In this study, PBL was simulated using a three-domain, two-way nested simulation of the WRF Model (version 3.2.1). ALH can be influenced by the transport of air mass and the convective dispersion of aerosols, both of which are usually associated with large-scale weather systems. Based on the different meteorological conditions, an automated workflow algorithm of ALH was constructed, and ALH was estimated by the meteorological parameters (relative humidity, temperature, wind speed and wind direction) from NCEP-FNL. The

155   detailed algorithm and the according calculations of PBL and ALH retrieval can be found in the He et al. (2016). The aerosol profiles were utilized to calculate the surface-level visibility from AOD, and the long-term spatial comparison with surface measurements over East China displayed that 90% of the samples exhibited correlation coefficients greater than 0.6 and that 68% of the samples exhibited correlation coefficients greater than 0.7 (He et al., 2016).

All of these multiplatform datasets with their spatial and temporal resolutions were summarized in Table 2. In this study,

160   bilinear interpolation was used in these datasets, and these datasets were interpolated to a spatial resolution of 0.1°×0.1° to collocate with the MODIS/AOD data. The ADRF simulation was also performed in each 0.1°×0.1° grid over East China. For temporal resolution, AOD and TOA radiation fluxes were from the MODIS and CERES sensor aboard the Terra satellite respectively, and they are available once per day. Both SSA and ERA-Interim are hourly means, surface albedo product in daily means. The ADRF simulations were only performed at the passing over of the Terra satellite under clear skies. The

165   temporal coverage is from 2000 to 2016. The research area and surface measurement sites for validation are shown in Figure 1.

3 Methodology

Clear-sky ADRF in the SW (0.25-4 μm) spectral region was simulated by the Santa Barbara Discrete Atmospheric Radiative Transfer (SBDART) model (Ricchiazzi et al., 1998). This model has been widely adopted for the estimation of aerosol radiative
170 forcing and validated with high accuracy (Li et al., 2010). In this study, SBDART model was used to estimate broadband SW (0.25-4 μm) surface irradiances and ADRF over East China. It is on the basis of the DISORT radiative transfer model, the low-resolution band models developed for LOWTRAN 7 atmospheric transmission, and the Mie scattering results for light scattering by water droplets and ice crystals (Ricchiazzi et al., 1998). Here, LOWTRAN 7 (Low Resolution Atmospheric Transmittance 7) solar spectrum was adopted in SBDART. This radiative transfer model also includes the standard aerosol
175 models derived from Shettle and Fenn (1975), in which aerosol optical parameters are wavelength dependence and the scattering parameters depend on the surface relative humidity. Users can also define different aerosol parameters in different wavelength. The default of the according spectral information is interpolated/extrapolated to all wavelengths using linear fitting on SSA/ASY, and using Ångstrom coefficients on AOD. According to Wang, P. et al. (2009), the input of aerosol parameters has very minor effect on the accuracy of irradiance simulation when using spectrally averaged values compared with detail
180 spectral information. Therefore, aerosol parameters (AOD, SSA, ASY) at 0.55 μm were used in the radiative transfer model. As for surface albedo, it is simply assumed that angular distribution of surface-reflected radiation is completely isotropic in the model. In our study, MODIS SW MCD43C3 (0.3-5 μm) product is used as albedo input, and it is nearly consistent with wavelength coverage (0.25-4 μm) of the output surface irradiances in SBDART.

As shown in Figure 2, the main inputs of SBDART model include aerosol properties (AOD from MODIS; SSA from MERRA-
185 2; ASY from the retrieval (Section 4.2)), surface albedo (from MODIS), aerosol vertical profile (from NCEP), atmospheric profiles (from ECMWF), total column ozone and water vapor (from ECMWF). The main outputs are radiative fluxes at the surface and TOA with and without aerosols. ADRF is defined as the difference in net radiative flux (downward minus upward) between aerosol and no-aerosol conditions. Here, we mainly concentrated on ADRF at the surface:

$$\mathrm{ADRF_{sur}} = (F \downarrow - F \uparrow) - (F_0 \downarrow - F_0 \uparrow), \qquad (1)$$

190 where F and F_0 represent radiative fluxes with and without the aerosol at the surface, respectively. The upward and downward arrows denote the directions of the radiative fluxes, which can be obtained by the outputs of SBDART. For simplicity, the upward radiative fluxes at the TOA are called F_u_toa, and the downward/upward radiative fluxes at the surface are called F_d_sur and F_u_sur, respectively (see Table 1 for the acronyms).

Besides above, Mann-Kendell (MK) test (Mann, 1945; Kendall, 1975) was used to calculate the trend of ADRF time series
195 and its significance level (above 90%) in our study. It identifies that whether monotonic trends exist in a time series and is widely employed for trend analysis of aerosol data. The detailed analysis produce can be found in Li et al. (2014). Prior to trend analysis, ADRF data were deseasonalized by subtracting the monthly mean during 2000-2016 to eliminate the influence of annual and seasonal cycles.

4 Results and discussion

4.1 Retrieval of aerosol properties

Before ADRF simulation, the accuracy of MERRA-2 SSA product, was evaluated firstly. In East China, six sunphotometer sites, Xuzhou (117.14ºE, 34.22ºN), Shouxian (116.78ºE, 32.56ºN), Hefei (117.16ºE, 31.91ºN), Taihu (120.22ºE, 31.42ºN), Pudong (121.79ºE, 31.05ºN) and Hangzhou (120.16ºE, 30.29ºN) (Figure 3a), were chosen for comparison with MERRA-2 SSA data.. The location of the sunphotometers was shown in Figure 3(a), and their geographical characteristics, observing periods, sample numbers as well as the fitted regression equation between MERRA-2 and sunphotometer SSA were presented in Table 3. Five sites (Xuzhou, Shouxian, Hefei, Taihu and Hangzhou) are AERONET sites and Level 1.5 inversion data of AERONET were used. The uncertainty of AERONET products can be found in Dubovik and King (2000). Another sunphotometer (CE318, Cimel Electronique, France) in Pudong was calibrated annually and maintained routinely, and a detailed description of calibration was presented in Cheng et al. (2015). The sunphotometer spectral products are available at wavelengths of 440, 675, 870, and 1020 nm, and they were interpolated at 0.55 μm to match MERRA-2 SSA. The collection time was constrained from 09:00 to 14:00 (local time), covering the overpass time of the Terra satellite. Meanwhile, the relatively high solar zenith in this period avoids possible inversion errors and improves the data accuracy (Tian et al., 2018b). Additionally, the specific MERRA-2 grid cell containing the sunphotometer was selected, and sunphotometer SSA was hourly averaged to match the MERRA-2 SSA product. The detailed comparisons at Xuzhou, Shouxian and Hefei were shown in Figure 3b. Orange dots represent Xuzhou samples and orange line is the according fitting curve, while the green represents Shouxian, and the black is Hefei. Figure 3c displays the comparison results at Taihu, Pudong and Hangzhou. Red denotes Taihu, the purple is Pudong and the yellow is Hangzhou. As shown in Figure 3, dashed lines are the range of ±10% relative error, all samples in Taihu, Pudong, Hefei, 94% of samples in Xuzhou, 93% in Shouxian and 98% in Hangzhou fall within the ±10% error. This finding suggests that MERRA-2 SSA agrees well with the sunphotometer data, even though few SSA samples are beyond the error range. Furthermore, the slopes of linear fitting curve are less than 1 at all sites except Shouxian (Table 3), and it reveals that MERRA-2 SSA has systematic biases at most area of East China. The primary reason for the discrepancy is the simple aerosol model assumption in MERRA-2 (Buchard et al., 2017). Only five aerosol types (sulfate, dust, sea salt, organic and black carbon) are involved; the lack of nitrate aerosols, which are highly scattering aerosols, may result in the underestimation of MERRA-2 SSA. In addition, the calibration errors among these instruments should be considered. Generally, the evaluation results in six sites show that the accuracy of MERRA-2 SSA product is acceptable in East China, with ±10% uncertainty.

After SSA was determined, ASY is the only unknown input parameter. ASY is the key to portraying the scattering direction of aerosols. ASY=1 denotes completely forward scattering, and ASY=0 is symmetric (Rayleigh) scattering. Here, gridded ASY was simulated by matching observed F_u_toa (from CERES) with simulated F_u_toa (from SBDART). The sensitivity test indicates that F_u_toa, just similar with F_u_sur (shown in Figure S3b), is a monotonically increasing function of ASY with other fixed inputs. Consequently, only one F_u_toa can be obtained by one specific ASY. In this premise, a binary search

was applied to approximate ASY to improve calculation efficiency (Chang, 2013). The goal of the binary search is to find the ASY when the simulated F_u_toa is close to the observed F_u_toa. To accomplish this, the ranges of F_u_toa are repeatedly diminished by taking the middle ASY as one of the boundary values, and when the difference between the F_u_toa observed by CERES and calculated by SBDART is less than 1, the corresponding approximation of ASY is finally obtained. The detailed scheme is illustrated in Figure 4. First, the value for ASY is initially assumed in the reasonable range of 0.1-0.9, and the upper and lower boundaries of ASY, along with other parameters, are input to SBDART to yield the initial range of calculated F_u_toa_a and F_u_toa_b. Then, this range is checked to determine whether it includes the F_u_toa (observed by CERES) by multiplying ((F_u_toa_a- F_u_toa)*(F_u_toa_b- F_u_toa)). If the multiplication result is negative, meaning that ASY falls within this range (ASYa, ASYb), the average of F_u_toa_a and F_u_toa_b is set as a new boundary (F_u_toa_c). Otherwise, this case is discarded, and the retrieval is not continued (ASY=NaN), perhaps due to inappropriate inputs. Next, for cases in which the multiplication result is negative, the multiplication process is applied to the new boundary ((F_u_toa_a- F_u_toa)*(F_u_toa_c- F_u_toa)). If this multiplication result is negative, the ASY falls within this range (ASYa, ASYc). Then, ASYc is set to represent ASYb. Otherwise, ASYc is set to represent ASYa. This process represents the scope-narrowing of the ASY boundary discussed above. With several iterations of narrowing the scope, the boundaries of the simulated F_u_toa become close to the true value of F_u_toa (observed by CERES). When the difference between the simulated F_u_toa boundary and the observed F_u_toa is less than 1, the corresponding ASY is considered as one approximation. In this process, the input parameters, including AOD (from MODIS), SSA (from MERRA-2), surface albedo (from MODIS), aerosol vertical profile (from NCEP), atmospheric profiles (from ECMWF), total column ozone and water vapor (from ECMWF), were input into the SBDART together in every iteration. All these inputs from 2000-2016 were used to simulate ADRF in each grid of East China. All calculations were performed on the Linux system. Following this method, ASY was retrieved in each grid cell over East China. The range of retrieved ASY is 0.50-0.80, and the mean ASY is 0.63, which is consistent with the observation site (Taihu) in East China (Xia et al., 2007). According to Mie theory, ASY is determined by the size distribution and the complex refractive index of aerosols. Therefore, the difference of ASY in East China can be partly related with the difference of fine mode radius. Xia et al. (2007) has reported that the fine mode volume median radius at Taihu site averages 0.181 μm over a range of AOD from 0.6-1.0, while it is 0.168 μm in northern China. In ASY retrieval, ASY is assumed to vary enough to match F_u_toa with ensuring the accuracy of all other inputs (e.g. AOD, SSA). This assumption can deviate from the reality if there are obvious differences between real and retrieval values of other inputs. This above condition can easily occur in the process of ASY retrieval, when ASY cannot be retrieved (ASY=NaN). Even if ASY can be obtained, ASY can be inaccurate when other inputs have large biases. The uncertainty of ASY caused by the other inputs (AOD, SSA, albedo, CERES F_u_toa) will be quantified in the following uncertainty analysis (Section 4.3).

After aerosol optical properties were obtained, these parameters from multiplatform datasets can be input into the SBDART model to simulate surface radiative fluxes and ADRF in East China according to the methodology in Section 3.

4.2 Validation of the method

265 Before conducting ADRF simulation in each grid of East China during 2000-2016, this method was first applied in the three grids of selected sites to assess the performance of ADRF retrieval. Three radiation sites in Baoshan (121.45°E, 31.4°N), Fuzhou (119.29°E, 26.08°N), Yong'an (117.37°E, 25.98°N) were chosen to make the comparisons between calculated F_d_sur and surface observation by the pyranometers (FS-S6, China) during 2014-2016. Red circles in Figure 1 denote the specific locations of pyranometers. Baoshan and Fuzhou are urban and coastal sites while Yong'an represents suburb and inland sites.

270 The different aerosol concentration levels and abundant aerosol types in these sites can represent the most of aerosol properties in East China. These pyranometers had regular maintenance and were calibrated annually through intercomparisons with the basic-reference station. Additionally, quality control has been performed at these sites according to Long and Shi (2008), including the removal of physical possible limits as determined by Baseline Surface Radiation Network (BSRN) and use of configurable limits based on climatological analysis of measurement data. The uncertainty in the pyranometers is expected to

275 be 5% (Song, 2013). Simulated F_d_sur was averaged in the scope of a 40 km side length with the center at the pyranometer, and the measured F_d_sur was averaged within ±30 min of the satellite overpass (Ichoku, et al., 2002).

Figure 5 displays the comparison results between simulated F_d_sur and observed F_d_sur by pyranometers at three sites. The simulated F_d_sur is fairly consistent with the observations, with correlation coefficients of 0.87 in Baoshan (Figure 5a) and Fuzhou (Figure 5b) and 0.90 in Yong'an (Figure 5c). Root mean squared error (RMSE) is a good indicator for measuring the

280 discrepancy between observed and simulated F_d_sur data. The RMSE is 7.9 W m^{-2} in Baoshan, 7.5 W m^{-2} in Fuzhou and 5.6 W m^{-2} in Yong'an. This discrepancy only accounts for 3-5% of ADRF, indicating that this retrieval method has a relatively higher accuracy than those in other studies (e.g., Thomas et al., 2013; Fu et al., 2017). Additionally, all slopes are less than 1, which implies that the method has systematic biases at these sites. A similar tendency was found in the comparison between MODIS AOD andsunphotometers in East China by He et al. (2010); it is speculated the main systematic error in ADRF

285 simulation may come from the input, MODIS AOD. Nevertheless, satisfactory comparison results indicate the suitability and feasibility of ADRF retrieval in the off/near the sea and urban/suburb sites of East China, although the type of underlying surface and aerosol properties are evidently different in these areas.

To further assess the discrepancy between simulated F_d_sur and the observations, the relative errors of each case at the three sites were calculated. The results suggest that underestimated cases (negative relative errors) account for 61% of the total cases

290 and overestimated cases (positive relative errors) account for 39%. According to the validation results, the sources of error in the simulation may be attributed to the following reasons:

Cloud contamination: An examination of cloudiness was carried out at the three sites. According to the empirical clear-sky detection method, one-hour radiation data of a pyranometer was used to discriminate clear-sky observations (Xia et al., 2007). The red dots in Figure 5 represent the cloudiness case detected by the pyranometer. Meanwhile, from the MODIS true color

295 map composed by channels 1, 4 and 3 (not shown), the olive green dots denote the specific case in which the site is completely covered by clouds. Taking one olive green cases (Baoshan, October 18, 2014) for an example. As shown in the Figure S2, it

is obvious that a large amount of cloud exists in the area of 29°N-31°N and 120°E-122°E, and Baoshan site is at the edge of the cloud. In this case, MODIS AOD was overestimated compared with sunphotometer AOD, this because some cloud effects were not completely removed from the MODIS/AOD calculation. Therefore, a large discrepancy can occur in these cases
300 between simulated F_d_sur and observation. The cloud effect, especially residual thin cirrus clouds, is difficult to completely remove from MODIS AOD (Kaufman et al., 2005). Moreover, the cloud mask algorithm in MODIS aerosol inversion sometimes fails to distinguish fog or haze in high-humidity conditions. Many more fog days can be observed in Fuzhou than the other two sites, and fogginess can significantly reduce the accuracy of the simulation (Ye et al. 2010). In addition, the error source of MODIS AOD is also from errors in the aerosol model assumption and surface reflectivity (Xie et al., 2011).

305 **Different spatial and temporal representativeness:** In the validation, the area measurement (satellite and reanalysis data) was compared to point measurements (pyranometer). For temporal matching, the pyranometer can capture the process of perturbation induced by air mass movement within one hour, whereas satellite can only provide the instantaneous condition. Hence, this comparison method inevitably introduces some degree of uncertainty.

Instrument and radiative transfer errors: One error source in pyranometers is the thermal offset effect. This spurious signal
310 is due to the difference in temperature between the inner dome and the detector of a pyranometer and can lead to additional errors in the irradiance measurements, especially diffuse irradiance (Sanchez et al., 2015). To reduce this effect, a pyranometer should be installed in a transparent ventilation hood. Alternatively, several statistical methods have also been proposed to suppress the thermal offset effect (e.g., Song, 2013; Cheng et al., 2014). In this study, the correction of the thermal offset was not performed because of the lack of additional observation data. Aside from the instrument error, the model simulation
315 discrepancy also depends on the radiative transfer models. They are based on some simplifications, including the sphericity of aerosol particles and the directional reflectance of the surface. Derimian et al. (2016) found that neglecting aerosol particle nonsphericity can overestimate the aerosol cooling effect. Furthermore, simulation results vary slightly among different models due to their different assumptions in radiative transfer. For instance, Yu et al. (2007) compared three models (second simulation of the satellite signal in the solar spectrum (6S), Moderate resolution atmospheric Transmission (MODTRAN) and SBDART)
320 at Xianghe station and showed that approximately 80% of the cases simulated by SBDART were lower than the surface observations, while the 6S simulation results were higher.

4.3 Sensitivity test and uncertainty analysis

To determine the uncertainty of the method for ADRF simulation caused by each input parameter, a sensitivity test for input parameters was carried out. A specific case in Shanghai on October 11, 2015, was used with the following values: AOD =
325 0.62, SSA = 0.85, ASY = 0.69, surface albedo = 0.13, total column water vapor = 0.69 g/cm^2, and total column ozone = 0.28 atm-cm. Figure S3 portrays the responses of F_d_sur, F_u_sur and ADRF to changes in one parameter while holding the other parameters constant. To remove the impact of units, all the parameters are dimensionless; that is, the ratio of the input to the actual value is used as the x-axis value. The absolute value of every slope describes the impact of every parameter on the dependent variables (F_d_sur, F_u_sur and ADRF). Figure S3 presents the actual condition of this case when the value of the

330   x-axis equals 1, in which F_d_sur is 629.15 W m^{-2}, F_u_sur is 83.52 W m^{-2}, and ADRF is -149.39 W m^{-2}. This situation denotes a strong cooling effect of aerosols at the surface. Apparently, different parameters impose diverse influences on the radiative values (F_d_sur, F_u_sur, and ADRF). As depicted in Figure S3, AOD, SSA, and ASY are three crucial parameters that greatly influence F_d_sur. Wang, P. et al. (2009) conducted the radiative closure experiment in the Netherlands and further found that, AOD can affect the changes of direct/diffuse irradiation, while SSA and ASY only affect the diffuse irradiance. For F_u_sur,

335   albedo, AOD, and SSA are more important parameters. The impact of surface albedo is much larger than the others because albedo actually determines how much of the irradiance is reflected by the surface. For ADRF, SSA, AOD, and ASY are major factors in determining ADRF. Additionally, only a large AOD produces much cooler at the surface, whereas increases in SSA and ASY can result in decreases in the aerosol cooling effect. In general, sensitivity test shows that ADRF depends highly on AOD, SSA, ASY and albedo. Two parameters (atmospheric profile and aerosol vertical profile) are not discussed because

340   these parameters have little impact on clear-sky ADRF in the above case. The atmospheric profile has a minor effect on the perturbations of ADRF compared with the total columns of atmospheric component (water vapor and ozone). This result has also been proven by Yu et al. (2007) and Li et al. (2016). As for aerosol profile, two typical shapes were input to SBDART for the sensitivity test. The first type (type I) has an elevated aerosol layer, and the second type (type II) is the two-layer aerosol model as mentioned above (Figure S1). The changes of the elevated layer height (type I) or PBL/ABL (type II) have very little

345   impact on ADRF, and the according maximum value of ADRF difference only can reach 0.5 W m^{-2}. This conclusion is consistent with Guan et al. (2009). However, this impact becomes much stronger in the presence of absorbing aerosols, especially in some extreme cases such as dust storms and biomass burning (Wang and Christopher, 2006). Reddy et al. (2013) also demonstrated that surface aerosol radiative forcing can be enhanced by 25% due to the insertion of the extinction profile of absorbing aerosols to replace the default profile.

350   On the basis of these four high-sensitivity factors, the uncertainties in ASY and ADRF due to these parameters were quantitatively assessed. According to data uncertainty mentioned in Section 2 and the SSA validation, the relative errors of AOD, SSA, albedo, and CERES F_u_toa are 20%, 10%, 5% and 1.6%, respectively. This lower/upper limit of parameter errors was input to the ADRF calculation, and the associated uncertainty was calculated by the difference between the simulated radiative flux with parameter errors and without errors. Notably, the uncertainty analysis is based on extreme conditions, and

355   the associated errors are much larger than the actual values. As displayed in Table 4, the uncertainty in ASY induced by SSA can reach up to 23%, indicating that SSA is a decisive factor in ASY retrieval when using CERES F_u_toa constraint. SSA also has the largest effect in regulating aerosol radiative forcing, which is consistent with the research on dust aerosols by Huang et al. (2009). AOD contributes uncertainties of 3.7% in ASY and 15.4% in ADRF. Albedo introduces 1.7~3.7% uncertainty in ASY and approximately 3% in ADRF. The error of CERES product produces approximately 1.7% uncertainty

360   in ASY and 1.5% in ADRF. The results of uncertainty analysis agree well with those of previous studies. For example, Xia et al. (2016) revealed that AOD and SSA together can account for 94% of surface ADRF. Zhuang et al. (2018) further noted that the error sources from the absorbing component of AOD and coarse-aerosol SSA contributed to the greater uncertainty in the ADRF. Therefore, improving the precision of the input parameter is helpful for obtaining reliable ADRF estimation. As

Michalsky et al. (2006) demonstrated, when using high-quality measurements as inputs to model, the biases between modeled and measured irradiance can decrease to 1.9%. In addition to these factors, Wang and Martin (2007) also revealed the effects of aerosol hygroscopicity on the aerosol phase function and the increase in SSA with RH enhancement, suggesting that relative humidity (RH) is also closely related to ADRF.

4.4 Long-term ADRF retrieval in East China

The above evaluations show the method for ADRF simulation is feasible and high-accuracy in East China, thus this method was further applied in each grid cell of East China to obtain a full coverage of ADRF during 2000-2016. Figure 6 outlines an overall picture of annual mean ADRF at the surface over East China during the past 17 years. It provides valuable information about aerosol radiative effect not only in the urban areas with intensive human activities, but also in the suburb with unavailable observational data. ADRFs in all grids are negative, ranging from -220 W m^{-2} to -20 W m^{-2}, implying that aerosols have cooling effect at the surface over East China. The yearly mean ADRF is -100.21 W m^{-2}. The magnitude of ADRF is higher than most cities in the world, such as Spain (Esteve et al., 2014), Gasan (Kim et al., 2006) and Karachi (Alam et al., 2011). The main reason is that AOD in East China is much larger than these cities, since East China has experienced rapid urbanization and economic development in the past 17 years and AOD is much larger than these regions. For example, mean AOD in East China is 0.62 in this study during 2003-2011 while AOD is 0.19 in Spain during 2003-2011 (Esteve et al., 2014). Red area denotes the high absolute value of ADRF (Figure 6), which are found in the densely populated and industrialized areas, including the western Shandong Province, YRD and Poyang Lake Plain. Low value (blue area) is observed in the Southern part, such as Fujian and southern Zhejiang Province. Obvious difference of ADRF distributions is found between the northern and southern part of East China, and the magnitude of ADRF increases from South to North. This pattern is consistent with site observations in Che et al., (2018), in which surface ADRF ranges from -150 to -100 W m^{-2} in the northern sites of East China (Huainan and Hefei in Anhui Province) while ADRF ranges from -100 to -50 W m^{-2} in the southern sites of East China (Jiande, ChunAn and Tonglu in Zhejiang Province). To further explore this difference, East China was divided into two parts: the North and South, with the boundary of 30° N. The occurrence frequencies of annual ADRF for each grid cell in the North and South were calculated in the Figure S4. The occurrence frequency shows a broad range from -300 W m^{-2} to 0 and the interval is 20 W m^{-2}. In the North, the largest proportion of ADRF, with the value of 76.47%, fall in the range of -100~-80 W m^{-2}, while the largest proportion (64.71%) of ADRF fall in the range of -60~-40 W m^{-2} in the South. The extreme value over -250 W m^{-2} may result from severe haze in the winter. Aerosol cooling radiative effect can sharply increase with large aerosol loadings. According to Yu et al. (2016b), surface ADRF can reach up to -263 W m^{-2} in the haze days, while in the non-haze days, it can decrease to -45 W m^{-2} in Beijing on January 2013. Usually in the heavy haze, the enhanced surface cooling, combined with atmosphere heating, can result in a more stable environment. It is unfavourable for the diffusion and dispersion of the aerosols, can further make air accumulation and enhance aerosol ADRF (Wu et al., 2016). Meanwhile, positive ADRF also found in few grid cells, although it is not shown in the Figure S4. This condition occurs over bright surface in East China especially with the abundance of absorbing aerosols (Sundström et al., 2015). According to the uncertainty analysis, ADRF is closely associated with the

12

inputs (SSA and AOD). Based on this, comparison was conducted among the mean spatial distribution of ADRF, AOD and SSA during 2000-2016 (Figure 7). It is clear to see that ADRF pattern is very similar to the negative phase of AOD pattern, that is, the areas of high AOD have low ADRF. As for SSA, the higher value can be found in the South than the North, which indicating the aerosols in the South are generally more scattering than the North. Therefore, the large difference between North and South can be mainly attributed to the difference in AOD. The industry locations and topography between the North and South are obviously different. With the development of economy and urbanization, large amounts of anthropogenic aerosols in the North can impose strong cooling radiative effect in the past two decades. It is worth noting that, although western Shandong has lower urbanization compared with YRD, aerosol cooling effect in western Shandong is even larger than in YRD. This is because Yimeng mountain (these mentioned places are all shown in Figure 1) located in the middle of Shandong, blocks the west flow, leading to the enhancement of the aerosol accumulations and high AOD near its western border (He et al., 2012b). Meanwhile, Shandong is also easily impacted by air pollution transported from North China. In addition, high absolute value of ADRF is also found in Poyang Lake in Jiangxi with abundance of anthropogenic aerosols, and these areas are surrounded by the mountains, the poor ventilation condition makes aerosols enhanced. Compared with the North, the South is characterized by more extensive vegetation coverage and less human activities, and AOD is relatively lower in the South (Figure 7b) and aerosols have weaker cooling effect.

Apart from spatial changes, temporal changes of ADRF during 2000-2016 were also analysed. Figure 8 displays the time series of monthly mean ADRF and AOD. For comparison, blue line represents ADRF and red line denotes AOD. They both show a fluctuation pattern, and they have an obvious negative phase with the correlation coefficient of 0.72. It indicates that the temporal change of ADRF is mainly attributed to the change of AOD. MK trends of ADRF and AOD are both positive but insignificant at 90% confident level, showing AOD and ADRF did not change significantly during 2000-2016 in East China. Paulot et al. (2018) also proved this insignificant trend of ADRF in China based on chemical-climate models. About AOD, Zhang et al. (2017) found that AOD trend increases since 2000-2007 and then decreases in the eastern China based on satellite observations. It is well known that the changes of AOD is closely linked with the change of anthropogenic emissions, especially in the developing country. Che et al. (2019) calculated that SO_2 is the dominant anthropogenic emissions factors to AOD in China during past few decades. Furtherly, model simulations also indicate the changes of sulfate aerosols are the largest contributor to AOD and aerosol effect in China (Paulot et al., 2018). MK trends of monthly mean ADRF in each grid cell during 2000-2016 were also calculated (Figure 9). Hatched regions indicate those exceeding the 90% significance level. It can be found high positive trend in Anhui and Jiangxi, indicating the aerosol cooling effect is weaker in this region during 2000-2016. However, a few regions experience the stronger of this cooling effect, especially in the northeast and south area of Yimeng mountain in Shandong. In general, the changes of ADRF during the past 17 years are mainly due to the anthropogenic emissions in East China. In addition, Paulot et al. (2018) further pointed that there is a nonlinear relationship between anthropogenic emissions and AOD/ADRF when considering the mix and oxidation of different emissions.

5 Conclusion

In this study, based on multiplatform datasets, high-accuracy ADRF distributions over East China during 2000-2016 were protrayed. MERRA-2 SSA data were first compared with sunphotometer data (Taihu, Xuzhou, Pudong), and the validation result shows that the relative error of the MERRA-2 SSA is ±10% over East China. Then, ASY in each grid was retrieved by matching the simulated F_u_toa by SBDART with satellite observations. Then, aerosol optical properties (AOD from MODIS, SSA from MERRA-2, and ASY from the retrieval), surface albedo (from MODIS), aerosol vertical profile (from NCEP), atmospheric profiles (from ECMWF), total column ozone and water vapor (from ECMWF) served as input parameters for SBDART to simulate ADRF in each grid cell of East China during 2000-2016. The validation result of this method at three sites (Baoshan, Fuzhou, and Yong'an) reveals that simulated F_d_sur is highly correlated with the pyranometer data during 2014-2016, with correlation coefficients of 0.87 in Baoshan and Fuzhou and 0.90 in Yong'an. The RMSEs are 7.9 W m^{-2} in Baoshan, 7.5 W m^{-2} in Fuzhou and 5.6 W m^{-2} in Yong'an. It shows that ADRF retrieval is feasible and has high accuracy over East China. In addition, associated factors, including cloud contamination, instrument and radiative transfer errors, as well as different spatial and temporal representativeness, were confirmed to produce additional uncertainty in ADRF simulations. Sensitivity test shows that ADRF depends highly on AOD, SSA, ASY and albedo. Uncertainty analysis shows the uncertainty in ADRF retrieval induced by SSA is calculated 24% and that by AOD is 15.4%. Finally, ADRF simulation was conducted in each grid of East China during 2000-2016. Long-term ADRF distributions over East China were presented for the first time. ADRFs in all grids are negative, the range of ADRF is between -220 W m^{-2} and -20 W m^{-2}, implying that aerosols have cooling effect on surface over East China. Aerosols are found to have stronger cooling effect in the North compared with the South. ADRF spatial pattern is consistent with the negative phase of AOD pattern, and the temporal changes of ADRF also have a close relationship with AOD. They indicate that the changes of ADRF in East China can mainly attributed to the changes of AOD. Furthermore, the spatiotemporal changes of AOD and ADRF are controlled by anthropogenic emissions, especially sulfate emissions in East China during past 17 years.

In summary, this study suggests that the method for ADRF retrieval is feasible in East China. Especially in suburbs with no monitoring resources, our study offers valuable information of direct radiative impact of aerosols. It is noted that, in our study, ADRF was calculated during the time that satellite passes by rather than the whole day. More additional observation data from the sites, are needed to further verify the performance of the ADRF retrieval and constrain these multiplatform datasets to improve the ADRF accuracy. In addition, it is necessary to improve the satellite instruments and the retrieval algorithm of aerosol properties; more novel methods, such as machine learning, can be involved in the ADRF estimates (Yin, 2010; Yu and Song, 2013). In the future work, aerosol-induced changes in the surface radiation under climate change and agricultural economic impact will be studied. This work can provide a deep understanding of aerosol radiative effects and is also helpful for aerosol modeling over East China.

References

Alam K., Trautmann T., and Blaschke T.: Aerosol optical properties and radiative forcing over mega-city Karachi. Atmospheric Research, 101(3):773-782, https://doi.org/10.1016/j.atmosres.2011.05.007, 2011.

Bellouin, N., Boucher, O., Haywood, J., and Reddy, M.: Global estimate of aerosol direct radiative forcing from satellite measurements, Nature, 438(7071), 1138-1141, https://doi.org/10.1038/nature04348,2005.

Buchard,V., Randles., C.A. Silva, A.M., Darmenov, A., Colarco, P. R., and Govindaraju, R.: The MERRA-2 aerosol reanalysis, 1980 onward. Part II: Evaluation and case studies, J. Clim., 30(17).6823, https://doi.org/10.1175/JCLI-D-16-0613.1, 2017.

Cescatti, A., Marcolla, B., Santhana Vannan, S.K., Pan, J.Y., Roman, M.O., Yang, X., Ciais, P,Cook, R., Law, B., Matteucci, G., Migliavacca, M., Moors, E., Richardson, A., Seufert, G., and Schaaf, C. : Intercomparison of MODIS albedo retrievals and in situ measurements across the global FLUXNET network, Remote Sens. Environ., 121, https://doi.org/10.1016/j.rse.2012.02.019, 2012.

Chameides, W., Yu, H., Liu, S., Bergin, M., Zhou, X., Mearns, L., Wang, G., Kiang, C., Saylor, R., Luo, C., and Huang, Y.: Case study of the effects of atmospheric aerosols and regional haze on agriculture: an opportunity to enhance crop yields in china through emission controls? Proc. Natl. Acad. Sci. U. S. A., 96(24), 13626-13633, https://doi.org/10.2307/121272, 1999.

Chang, Shi-Kuo.: Data structures and algorithms. Software Engineering and Knowledge Engineering. 13. Singapore: World Scientific. ISBN 978-981-238-348-8, 2003.

Chang, W., and Liao, H.: Anthropogenic direct radiative forcing of tropospheric ozone and aerosols from 1850 to 2000 estimated with IPCC AR5 emissions inventories, Atmos. Oce. Sci. Lett., 2 (4): 201–207, https://doi.org/10.1080/16742834.2009.11446804, 2009.

Che, H., Zhang, X., Chen, H., Damiri, B., and Zhou, T.: Instrument calibration and aerosol optical depth validation of the China aerosol remote sensing network, J. Geophys. Res. Atmos., 114(D3), D03206, https://doi.org/10.1029/2008jd011030, 2009.

Che, H., Qi, B., Zhao, H., Xia, X., Eck, T. F., Goloub, P., Dubovik, O., Estelles, V., Cuevas-Agulló, E., Blarel, L., Wu, Y., Zhu, J., Du, R., Wang, Y., Wang, H., Gui, K., Yu, J., Zheng, Y., Sun, T., Chen, Q., Shi, G., and Zhang, X.: Aerosol optical properties and direct radiative forcing based on measurements from the China Aerosol Remote Sensing Network (CARSNET) in eastern China, Atmos. Chem. Phys., 18, 405-425, https://doi.org/10.5194/acp-18-405-2018, 2018.

Che, H., Xia, X., Zhao, H., Dubovik, O., Holben, B. N., Goloub, P., Cuevas-Agulló, E., Estelles, V., Wang, Y., Zhu, J., Qi, B., Gong, W., Yang, H., Zhang, R., Yang, L., Chen, J., Wang, H., Zheng, Y., Gui, K., Zhang, X., and Zhang, X.: Spatial distribution of aerosol microphysical and optical properties and direct radiative effect from the China Aerosol Remote Sensing Network, Atmos. Chem. Phys. Discuss., https://doi.org/10.5194/acp-2019-405, in review, 2019.

Cheng, T., Xu, C., Duan, J., Wang, Y., Leng, C., Tao, J., Che, H., He, Q., Wu, Y., Zhang, R., Li, X., Chen, J., Kong, L., and Y., X., Seasonal variation and difference of aerosol optical properties in columnar and surface atmospheres over Shanghai, Atmos. Environ., 123, 315-326, https://doi.org/10.1016/j.atmosenv.2015.05.029, 2015.

Cheng, X., Ding, L., Yang, Y., Bai, S., Zhou, H., Peng, J., Quan, J., and Song, J.: Correction methods for thermal offset errors in TBQ-2-B pyranometers, J. Trop. Meteoro., 20(4), 375-385, https://doi.org/10.16555/j.1006-8775.2014.04.011, 2014.

Chu, D. A., Kaufman, Y. J., Ichoku, C., Remer, L. A., Tanré, D., and Holben, B. N.: Validation of MODIS aerosol optical depth retrieval over land, Geophys. Res. Lett., 29(12), 1617−1621, https://doi.org/10.1029/2001gl013205, 2002.

Chung, C. E., Chu, J. E., Lee, Y., Van Noije, T., Jeoung, H., Ha, K. J., and Marks, M.: Global fine-mode aerosol radiative effect as constrained by comprehensive observations, Atmos. Chem. Phys.,16(13), 8071-8080, https://doi.org/10.5194/acp-16-8071-2016,2016.

Colarco, P., Silva, A. D., Chin, M., Diehl, T.: Online simulations of global aerosol distributions in the NASA GEOS-4 model and comparisons to satellite and ground-based aerosol optical depth, J. Geophys. Res. Atmos., 115(D14), https://doi.org/10.1029/2009JD012820, 2010.

Dee, D. P., Uppala, S. M., Simmons, A. J., Berrisford, P., Poli, P., Kobayashi, S. Andrae, U., Balmaseda, M. A., Balsamo, G., Bauer, P., Bechtold, P., Beljaars, A. C. M., van de Berg, L., Bidlot, J., Bormann, N., Delsol, C., Dragani, R., Fuentes, M., Geer,

16

A. J., Haimberger, L., Healy, S. B., Hersbach, H., Hólm, E. V., Isaksen, L., Kållberg, P., Köhler, M., Matricardi, M., McNally, A. P., Monge-Sanz, B. M., Morcrette, J.J., Park, B.K., Peubey, C., de Rosnay, P., Tavolato, C., Thépaut, J.-N., and Vitart, F.:

530   The ERA‑Interim reanalysis: Configuration and performance of the data assimilation system, Q. J. R. Meteorol. Soc., 137(656), 553- https://doi.org/10.1002/qj.828, 2011.

De Graaf, M., Stammes., P., and Tilstra, L. G.: Quantification of the aerosol direct radiative effect from smoke over clouds using passive space-borne spectrometry, AIP Conference Proceedings 1531, 640, https://doi.org/10.1063/1.4804851, 2013.

Derimian, Y., Dubovik, O., Huang, X., Lapyonok, T., Litvinov, P., Kostinski, A. B., Dubuisson, P., and Ducos, F.:

535   Comprehensive tool for calculation of radiative fluxes: illustration of shortwave aerosol radiative effect sensitivities to the details in aerosol and underlying surface characteristics, Atmos. Chem. Phys., 16(9), 5763-5780, https://doi.org/10.5194/acp-16-5763-2016, 2016.

Dubovik, O. and King, M.: A flexible inversion algorithm for retrieval of aerosol optical properties from Sun and sky radiance measurements, J. Geophys. Res. Atmos.,105, 20673–20696, https://doi.org/10.1029/2000jd900282, 2000.

540   Dubovik, O., Z. Li, M.I. Mishchenko, D. Tanré, Y. Karol, B. Bojkov, B. Cairns, D.J. Diner, W.R. Espinosa, P. Goloub, X. Gu, O. Hasekamp, J. Hong, W. Hou, K.D. Knobelspiesse, J. Landgraf, L. Li, P. Litvinov, Y. Liu, A. Lopatin, T. Marbach, H. Maring, V. Martins, Y. Meijer, G. Milinevsky, S. Mukai, F. Parol, Y. Qiao, L. Remer, J. Rietjens, I. Sano, P. Stammes, S. Stamnes, X. Sun, P. Tabary, L.D. Travis, F. Waquet, F. Xu, C. Yan, and D. Yin: Polarimetric remote sensing of atmospheric aerosols: instruments, methodologies, results, and perspectives, J. Quant. Spectrosc. Radiat. Transfer, 224, 474-511,

545   https://doi.org/10.1016/j.jqsrt.2018.11.024, 2019.

Esteve A R, Estellés, V, Utrillas, María P, and Martínez-Lozano J.A.: Analysis of the aerosol radiative forcing over a Mediterranean urban coastal site. Atmos. Res., 137,195-204. http://dx.doi.org/10.1016/j.atmosres.2013.10.009, 2014.

Fu, Y., Zhu, J., Yang, Y., Yuan, R., Liu, G., Xian, T., and Liu, P.: Grid-cell aerosol direct shortwave radiative forcing calculated using the SBDART model with MODIS and AERONET observations: an application in winter and summer in eastern China,

550   Adv. Atmos. Sci., 34(8), 952-964, https://doi.org/10.1007/s00376-017-6226-z, 2017.

Gelaro, R., McCarty, W., Suarez, M. J., Todling, R., Molod, A., Takacs, L., Randles, C., Darmenov, A., Bosilovich, M., and Reichle, R.: The modern-era retrospective analysis for research and applications, version 2 (MERRA-2), J. Clim., 30(14), 5419-5454, https://doi.org/10.1016/10.1175/JCLI-D-16-0758.1, 2017.

Gong, F., Xin, J., Wang, S., Wang Y., and Zhang, T.: Anthropogenic aerosol optical and radiative properties in the typical

555   urban/suburban regions in China, Atmos. Res., 197(15)177-187, https://doi.org/10.1016/j.atmosres.2017.07.002, 2017.

Guan, H., Schmid, B., Bucholtz, A., and Bergstrom, R.: Sensitivity of shortwave radiative flux density, forcing, and heating rate to the aerosol vertical profile, J. Geophys. Res. Atmos., 115, https://doi.org/10.1029/2009JD012907, 2010.

Haywood, J., and Boucher, O.: Estimates of the direct and indirect radiative forcing due to tropospheric aerosols: a review, Rev. Geophys., 38(4), 513, https://doi.org/10.1029/1999rg000078, 2000.

560   He, Q., Li, C., Mao, J., Lau, A., and Chu, D.: Analysis of aerosol vertical distribution and variability in Hong Kong, J. Geophys. Res., 113, D14211, https://doi.org/10.1029/2008JD009778, 2008.

He, Q., Li, C., Tang, X., Li, H., Geng, F., and Wu, Y.: Validation of MODIS derived aerosol optical depth over the Yangtze River Delta in China, Remote Sens. Environ. 114(8), 1649-1661, https://doi.org/10.1016/j.rse.2010.02.015, 2010.

He, Q., Li, C., Geng, F., Yang, H, Li, P., Li, T., Liu, D., and Pei, Z.: Aerosol optical properties retrieved from sun photometer measurements over Shanghai, China, J.Geophy. Res. Atmos., 117(D16), https://doi.org/10.1029/2011JD017220, 2012a.

He, Q., Li, C., Geng, F., Lei, Y., and Li, Y.: Study on long-term aerosol distribution over the land of East China using MODIS data, Aerosol Air Qual. Res.12,300-315, https://doi.org/10.4209/aaqr.2011.11.0200, 2012b.

He, Q., Li, C., Geng, F., Zhou, G., Gao, W., Yu, W., Li, Z., and Du, M.: A parameterization scheme of aerosol vertical distribution for surface-level visibility retrieval from satellite remote sensing. Remote Sens. Environ., 181, 1-13, https://doi.org/10.1016/j.rse.2016.03.016, 2016.

Hess, M.: Optical properties of aerosols and clouds: the software package OPAC, Bull. Am. Meteorl. Soc., 79(5), 831-844. https://doi.org/10.1175/1520-0477(1998)079<0831:OPOAAC>2.0.CO;2, 1998.

Holben, B. N., Tanré, D., Smirnov, A., Eck, T. F., Slutsker, I., Abuhassan, N., Newcomb, W. W., Schafer, S., Chatenet, B., Lavenu, F., Kaufman, Y., Vande, J., Setzer, A., Markham, B., Clark, D., Frouin, R., Halthore, R., Karneli, A., O'Neill, N., Pietras, C., Pinker, R., Voss, K., and Zibordi, G.: An emerging ground-based aerosol climatology: aerosol optical depth from AERONET, J. Geophys. Res. Atmos. 106(D11), 12067-12097, https://doi.org/10.1029/2001JD900014, 2001.

Huang, J., Fu, Q., Su, J., Tang, Q., Minnis, P., Hu, Y., Yi. Y, and Zhao. Q.: Taklimakan dust aerosol radiative heating derived from CALIPSO observations using the Fu-Liou radiation model with CERES constraints, Atmos. Chem. Phys., 9(12),4011-4021, https://doi.org/10.5194/acp-9-4011-2009, 2009.

Ichoku, C., Chu, D., Mattoo, S., Kaufman, Y., Remer, L. A , Tanré, D., Slutsker, I, and Holben N.: A spatio-temporal approach for global validation and analysis of MODIS aerosol products, Geophys. Res. Lett., 29(12), MOD1-1–MOD1-4, https://doi.org/10.1029/2001GL013206，2002.

IPCC: Fifth Assessment Report: Climate Change 2013, Cambridge University Press, New York, NY, USA, 2013.

José A. Ruiz-Arias, Dudhia, J., Santos-Alamillos, F., and David Pozo-Vázquez.: Surface clear-sky shortwave radiative closure intercomparisons in the weather research and forecasting model, J. Geophys. Res. Atmos., 118(17), 9901-9913, https://doi.org/10.1002/jgrd.50770, 2013.

Kaufman, Y. J., Tanre, D. L., Remer, A., Vermote, E. F., Chu, A., and Holben, B. N.: Operational remote sensing of tropospheric aerosol over land from EOS moderate resolution imaging spectroradiometer, J. Geophys. Res., 102,17051–17067, https://doi.org/10.1029/96jd03988, 1997.

Kaufman, Y. J., Remer, L. A. , Tanre, D. , Li, R. R. , Kleidman, R. , Mattoo, S. , Levy, R., Eck, T. Holben, B., Ichoku, C., Martins, J., and Koren, I.: A critical examination of the residual cloud contamination and diurnal sampling effects on MODIS estimates of aerosol over ocean, IEEE Trans. Geosci. Remote Sens., 43(12), 2886-2897, https://doi.org/10.1109/tgrs.2005.858430, 2005.

Kendall, M. G.: Rank Correlation Methods, Griffin, London, 1975.

595   Kim, J., Yoon S. C., Kim S. W., Brechtel, F., Jefferson, A., Dutton, E.G., Bower, K.N., Cliff, S. and Schauer., J.: Chemical apportionment of shortwave direct aerosol radiative forcing at the Gosan super-site, Korea during ACE-Asia. Atmospheric Environment, 40(35):6718-6729. https://doi.org/10.1016/j.atmosenv.2006.06.007, 2006.

Levelt, P., G. van den Oord, M. Dobber, A. Malkki, H. Visser, J. de Vries, P. Stammes, J. Lundell, and H. Saari.:The Ozone Monitoring Instrument, IEEE Transactions on Geoscience and Remote Sensing 44 (5): 1093–1101.
600   https://doi.org/10.1109/TGRS.2006.872333,2006.

Levy, R. C., Mattoo, S., Munchak, L. A., Remer, L. A., Sayer, A. M., and Hsu, N.C.: The Collection 6 MODIS aerosol products over land and ocean, Atmos. Meas. Tech. 6, 2989-3034, https://doi.org/10.5194/amtd-6-159-2013, 2013.

Li, J., Carlson, B. E., Dubovik, O., and Lacis, A. A.: Recent trends in aerosol optical properties derived from AERONET measurements, Atmos. Chem. Phys., 14, 12271–12289, https://doi.org/10.5194/acp-14-12271-2014,2014.

605   Loeb, N. G., Kato, L. S., Loukachine, K., and Manalo-Smith, N.: Angular distribution models for Top-of-Atmosphere radiative flux estimation from the Clouds and the Earth's Radiant Energy System instrument on the Terra satellite, Part I: Methodology, J. Appl. Meteor., 42(4), 338., 22, 338–351, https://doi.org/10.1175/JTECH1712.1, 2003.

Long, C. N. and Shi, Y.: An automated quality assessment and control algorithm for surface radiation measurements, The Open Atmospheric Science Journal, 2, 23–37, https://doi.org/10.2174/1874282300802010023, 2008.

610   Li, C., Mao, J., Lau, A., Yuan, Z., Wang. M., and Liu, X.: Characteristics of distribution and seasonal variation of aerosol optical depth in Eastern China with MODIS products (in Chinese). Chin. Sci. Bull. 48(22),2488-2495, https://doi.org/10.1360/03wd0224, 2003.

Li X., Sheng L., Liu, Q., Liu Y., and Wang L.: Error in calculation of surface radiation based on SBDART radiative transfer model (in Chinese), Period. Ocean Uni. Chin. 46(8), 13-18, 2016.

615   Li, Z., Lee, K., Wang, Y., Xin, J., and Hao, W.: First observation-based estimates of cloud-free aerosol radiative forcing across China, J. Geophys. Res., 115, D00K18, https://doi.org/10.1029/2009jd013306, 2010.

Liu, J., Zheng, Y., Li, Z., Flynn, C., and Cribb, M.: Seasonal variations of aerosol optical properties, vertical distribution and associated radiative effects in the Yangtze Delta region of China, J. Geophys. Res-Atmos., 117(D16), https://doi.org/10.1029/2011JD016490, 2012.

620   Liao, H., Chang, W., and Yang, Y.: Climatic effects of air pollutants over china: a review, Adv. Atmos. Sci. 32(1), 115-139, https://doi.org/10.1007/s00376-014-0013-x, 2015.

Long, C. N. and Shi, Y.: An automated quality assessment and control algorithm for surface radiation measurements, The Open Atmospheric Science Journal, 2, 23–37, https://doi.org/10.2174/1874282300802010023, 2008.

Mann, H. B.: Nonparametric tests against trend, Econometrica , 13, 245–259, 1945.

625   Menon, S., Hansen, J., Nazarenko, L., and Luo, Y.: Climate effects of black carbon aerosols in China and India, Science, 297, https://doi.org/10.1126/science.1075159, 2002.

Michalsky, J., Anderson, G., Barnard, J., Delamere, J., Gueymard, C., Kato, S., Kiedron, P., Mc Comiskey, A., and Ricchiazzi, P.: Shortwave radiative closure studies for clear skies during the atmospheric radiation measurement 2003 aerosol intensive observation period, J. Geophys. Res. Atmos., 111(D14), https://doi.org/10.1029/2005JD006341, 2006.

630 Nyeki, S., Wehrli, C., Gröbner, J., Kouremeti, N., Wacker, S., Labuschagne, C., Mbatha, N., and Brunke, G.: The GAW-PFR aerosol optical depth network: the 2008-2013 time series at Cape Point Station, South Africa, J. Geophys. Res. Atmos., 120(10), 5070-5084, https://doi.org/10.1002/2014JD022954, 2015.

Oikawa, E., Nakajima, T., Inoue, T., and Winker, D.: A study of the shortwave direct aerosol forcing using ESSP/CALIPSO observation and GCM simulation, J. Geophys. Res. Atmos., 118, 3687–3708, https://doi.org/10.1002/jgrd.50227, 2013.

635 Paulot, F., Paynter, D., Ginoux. P., Naik, V., and Horowitz, L. W.: Changes in the aerosol direct radiative forcing from 2001 to 2015: observational constraints and regional mechanisms, Atmos. Chem. Phys., 18, 13265–13281, https://doi.org/10.5194/acp-18-13265-2018, 2018

Qiu, Y., Liao, H., Zhang, R., and Hu, J.: Simulated impacts of direct radiative effects of scattering and absorbing aerosols on surface-layer aerosol concentrations in China during a heavily polluted event in February 2014: aerosol radiative feedbacks 640 over the NCP, J. Geophys. Res. Atmos., 122, https://doi.org/10.1002/2016JD026309, 2017.

Randles, C. A. , Sliva, A. M. D. , Buchard, V. , Colarco, P. R. , and Flynn, C. J.: The MERRA-2 Aerosol Reanalysis, 1980 – onward, Part I: System Description and Data Assimilation Evaluation, J. Clim., 30(17), 6823, https://doi.org/10.1175/JCLI-D-16-0609.1, 2017.

Reddy, K., Kumar, D., Ahammed, Y., and Naja, M.: Aerosol vertical profiles strongly affect their radiative forcing 645 uncertainties: study by using ground-based lidar and other measurements, Remote Sens. Lett., 4(10), 1018-1027, https://doi.org/10.1080/2150704X.2013.828182, 2013

Ricchiazzi, P., S. R. Yang, C. Gautier, and D. S.: SBDART: A research and teaching software tool for plane parallel radiative transfer in the Earth's atmosphere, Bull. Am. Meteorl. Soc., 79, 2101–2114, https://doi.org/10.1175/1520-0477(1998)0792.0.CO;2, 1998.

650 Rosenfeld, D.: TRMM observed first direct evidence of smoke from forest fires inhibiting rainfall, Geophys. Res. Lett., 26, 3105-3108, https://doi.org/10.1029/1999gl006066, 1999.

Sanchez, G., Serrano, A., Cancillo, M., and Garcia, J.: Pyranometer thermal offset: measurement and analysis, J. Atmos. Ocean. Technol., 32(2), 234-246, https://doi.org/10.1175/jtech-d-14-00082.1, 2015.

Shettle, E. P., and R. W. Fenn, 1975: Models of the atmospheric aerosols and their optical properties. AGARD Conf. Proc., 655 Optical Propagation in the Atmosphere, Lyngby, Denmark, NATO Advisory Group for Aerospace Research, 2.1-2.16

Song, J. Y., Quality Evaluations and feature analysis of radiation data at background stations in China, Master thesis, Chinese Academy of Meteorological Sciences, 2013.

Song, Z., Fu, D., Zhang, X., Wu, Y., Xia, X., and He, J.: Diurnal and seasonal variability of PM2.5 and AOD in North China plain: Comparison of MERRA-2 products and ground measurements, Atmos. Environ., 191,70-78, 660 https://doi.org/10.1016/j.atmosenv.2018.08.012, 2018.

Su, W., Corbett, J., Eitzen, Z., and Liang, L.: Next-generation angular distribution models for top-of-atmosphere radiative flux calculation from CERES instruments: methodology, Atmos. Meas. Tech., 8(2), 611-632, https://doi.org/10.5194/amtd-8-4489-2015, 2015.

665 Sundström, A., Arola, A., Kolmonen, P., Xue, Y., De Leeuw, G., and Kulmala, M. On the use of a satellite remote-sensing-based approach for determining aerosol direct radiative effect over land: a case study over China, Atmos. Chem. Phys., 15(1), 505-518, https://doi.org/10.5194/acp-15-505-2015, 2015.

Tian, P., Zhang, L., Cao, X., Sun, N., and Wang, H.: Enhanced bottom-of-the-atmosphere cooling and atmosphere heating efficiency by mixed-type aerosols: a classification based on aerosol nonsphericity, J. Atmos. Sci., 75(1), 113-124, https://doi.org/10.1175/JAS-D-17-0019.1, 2018a.

670 Tian, P., Zhang, L., Ma, J., Tang, K., Xu, L., Wang, Y., Cao, X., Liang, J., Ji, Y., Jiang, H., and Zhang, R.: Radiative absorption enhancement of dust mixed with anthropogenic pollution over east Asia, Atmos. Chem. Phys., 18(11), 7815-7825, https://doi.org/10.5194/acp-18-7815-2018, 2018b.

Tilstra, L. G., and Stammes P. . : Earth reflectance and polarization intercomparison between SCIAMACHY onboard Envisat and POLDER onboard ADEOS-2, J. Geophys. Res., 112, D11304, https://doi.org/10.1029/2006JD007713,2007.

675 Twomey, S.: The influence of pollution on the shortwave albedo of clouds, J. Atmos. Sci., 34, 1149-1152, https://doi.org/10.1175/1520-0469(1977)034<1149:TIOPOT>2.0.CO;2. , 1977.

Thomas, G. E., Chalmers, N., Harris, B., Grainger, R. G., and Highwood, E. J.: Regional and monthly and clear-sky aerosol direct radiative effect (and forcing) derived from the GlobAEROSOL-AATSR satellite aerosol product, Atmos. Chem. Phys., 13(1), 393-410, https://doi.org/10.5194/acp-13-393-2013, 2013.

680 Wang, J., and Christopher, S.: Mesoscale modeling of central american smoke transport to the United States: 2. smoke radiative impact on regional surface energy budget and boundary layer evolution, J. Geophys. Res., 111(D14), D14S92, https://doi.org/10.1029/2005JD006720, 2006.

Wang, J., and Martin. T.: Satellite characterization of urban aerosols: importance of including hygroscopicity and mixing state in the retrieval algorithms, J. Geophys. Res., 112, D17203, https://doi.org/10.1029/2006JD008078, 2007.

685 Wang, J., Van, d., and Reid, J.: A conceptual model for the link between Central American biomass burning aerosols and severe weather over the South Central United States, Environ. Res. Lett., 4(1), 015003, https://doi.org/10.1088/1748-9326/4/1/015003, 2009.

Wang, P., W. H. Knap, P. Kuipers Munneke, and P. Stammes.: Clear-sky shortwave radiative closure for the Cabauw Baseline Surface Radiation Network site, Netherlands, J. Geophys. Res., 114, D14206, https://doi.org/10.1029/2009JD011978, 690 2009.

Wang, X., Dickinson, R., Su, L., Zhou, C., and Wang, K.: PM2.5 pollution in China and how it has been exacerbated by terrain and meteorological conditions, Bull. Am. Meteorl. Soc., 99(1), 105-120, https://doi.org/10.1175/BAMS-D-16-0301.1, 2018.

Wang, Y., Xin, J., Pan, Y., Ji, D., Liu, Z., Wen, T., Wang, Y., Li, X., Sun, Y., Wang, P., Wang, G., Wang, X., Cong, Z., Song, T., Hu, B., Wang, L., Tang, W., Gao, W., Guo, Y., Miao, H., Tian, S., and Wang, L.: The campaign on atmospheric aerosol

695 research network of China: Care-China, Bull. Am. Meteorl. Soc., 141104074432007, https://doi.org/10.1175/BAMS-D-14-00039.1, 2014.

Wang, Y., Duan, J., Xie, X., He, Q., Cheng, T., Mu, H., Gao, W., and Li, X.: Climatic factors and their availability in estimating long-term variations of fine particle distributions over East China, J. Geophys. Res. Atmos., 124, https://doi.org/10.1029/2018JD029622, 2019.

700 Wu, Y., Zhang, J., Zhang, R., and Zhang, X.: Ground-based remote sensing of aerosol climatology in China: aerosol optical properties, direct radiative effect and its parameterization, Atmos. Environ., 124(2015), 243-251, https://doi.org/10.1016/j.atmosenv.2015.05.071, 2016.

Xia, X., Chen, H., Li, Z., Wang, P., and Wang, J.: Significant reduction of surface solar irradiance induced by aerosols in a suburban region in northeastern China, J. Geophys. Res. Atmos., 112(D22S02), https://doi.org/10.1029/2006JD007562, 2007.

705 Xia, X., Che, H., Zhu, J., Chen, H., Cong, Z., Deng, X., Fan, X., Fu, Y., Goloub, P., Jiang, H., Liu, Q., Mai, B., Wang, P.,Wu, J., Bei, N., Hu, B., Liu, S., Zhou, M., Wang, Q., Li, X., Liu, L., Feng, T., Liu, Z., Wang, Y., Cao, J., Tie, X., Wang, J., Molina, L. T., and Li, G.: Aerosol–radiation feedback deteriorates the wintertime haze in the North China Plain, Atmos. Chem. Phys., 19, 8703-8719, https://doi.org/10.5194/acp-19-8703-2019, 2019.

Xia, X., Z. Li, B. Holben, P. Wang, T. Eck, H. Chen, M. Cribb, and Y. Zhao: Aerosol optical properties and radiative effects 710 in the Yangtze Delta region of China, J. Geophys. Res., 112, D22S12, https://doi.org/10.1029/2007JD008859,2007.

Xie, Y., Zhang, Y., Xiong, X., Qu, J., and Che, H.: Validation of MODIS aerosol optical depth product over china using CARSNET measurements, Atmos. Environ., 45(33), 5970-5978, https://doi.org/10.1016/j.atmosenv.2011.08.002, 2011.

Xin, J., Wang, Y., Li, Z., Wang, P., and Hu, B.: Aerosol optical depth (AOD) and Ångström exponent of aerosols observed by the Chinese sun hazemeter network from August 2004 to September 2005, J. Geophys. Res. Atmos., 112(D5), 1703-1711, 715 https://doi.org/10.1029/2006JD007075, 2007.

Ye, G., Wu, Y., and Liu, B.: Spatial and temporal distribution characteristics of fog and haze in Fuzhou (in Chinese), Chin. Environ. Science Technol. v.33(10), 114-119, 2010.

Yin, K., Cloud computing: Concept, model, and key technologies, ZTE Technology Journal, 16(4),18-23,2010

Yu, H., Dickinson, R., Chin, M., Kaufman, Y., Zhou, M., Tian, Y., Dubovik, O., and Holben, B.: direct radiative effect of 720 aerosols as determined from a combination of MODIS retrievals and GOCART simulations, J. Geophys. Res.,109, D03206, https://doi.org/10.1029/2003JD003914

Yu, H., Kaufman, Y. J., Chin, M., Feingold, G., Remer, L. A., Anderson, T. L., Balkanski, Y., Bellouin, N., Boucher, O., Christopher, S., Decola, P., Kahn, R., Koch, D., Loeb, N., Reddy, M. S., Schulz, M., Takemura, T., and Zhou, M.: A review of measurement-based assessments of the aerosol direct radiative effect and forcing, Atmos. Chem. Phys., 6(3), 613-666, 725 https://doi.org/10.5194/acp-6-613-2006, 2006.

Yu, X., Ma, J., Kumar, R., K. Zhu, B., An, J., He, J., and Li, M.: Measurement and analysis of surface aerosol optical properties over urban Nanjing in the Chinese Yangtze River Delta, Sci. Total Environ., 542, 277-291, https://doi.org/10.1016/j.scitotenv.2015.10.079, 2016a.

Yu, X., Kumar, K., Lyu R., and Ma, J.: Changes in column aerosol optical properties during extreme haze-fog episodes in January 2013 over urban Beijing, Environ. Pollut., 210, 217-226, https://doi.org/10.1016/j.envpol.2015.12.021, 2016b.

Yu, Y., Xia, X., and Chen, H.: A comparison between measured and modeled clear-sky surface solar irradiance (in Chinese), Aeta Energiae Solaris Sinica, 28(3): 233-240, 2007.

Yu, Y., and Song, M.: Big data (3), ZTE Technology Journal. 19(3), 57-62, https://doi.org/10.3969/j.issn.1009-6868.2013.03.013, 2013

Zhang, J. L., Reid, S. J., Contreras, R. A., and Xian, P.: Has China been exporting less particulate air pollution over the past decade? Geophys. Res.Lett., 44, https://doi.org/ 10.1002/2017GL072617, 2017.Zhou, C., Zhang, H., Zhao, S., and Li, J.: On effective radiative forcing of partial internally and externally mixed aerosols and their effects on global climate, J. Geophys. Res. Atmos., 123, https://doi.org/10.1002/2017JD027603, 2018.

Zhang, M., Ma, Y., Gong, W., Liu, B., Shi, Y., and Chen, Z.: Aerosol optical properties and radiative effects: assessment of urban aerosols in central China using 10-year observations, Atmos. Environ.,182, 275-285, https://doi.org/10.1016/j.atmosenv.2018.03.040, 2018.

Zhuang, B., Wang, T., Liu, J., Che, H., Han, Y., Fu, Y., Li, S., Xie, M., Li, M., Chen, P., Chen, H., Yang, X., and Sun, J.: The optical properties, physical properties and direct radiative forcing of urban columnar aerosols in the Yangtze River Delta, China, Atmos. Chem. Phys., 18(2), 1419-1436, https://doi.org/10.5194/acp-18-1419-2018, 2018.

Table 1: Summary of the acronyms.

ADRF	Aerosol direct radiative forcing (W m^{-2})
SSA	Single scattering albedo (unit less)
ASY	Asymmetry parameter (unit less)
AOD	Aerosol optical depth (unit less)
F_u_toa	Upward radiative fluxes at the top of atmosphere (W m^{-2})
F_d_sur	Downward radiative fluxes at the surface (W m^{-2})
F_u_sur	Upward radiative fluxes at the surface (W m^{-2})

Table 2: Satellite and reanalysis datasets used in the study.

Parameters	Products	Sensors/Models	Spatial Resolution	Temporal Resolution
AOD	MOD04 L2	Terra MODIS	0.1°×0.1°	instantaneous
SSA	tavg1_2d_aer_Nx	MERRA-2	0.625°×0.5°	hourly
Surface albedo	MCD43C3	Terra+Aqua MODIS	0.05°×0.05°	daily
Upward TOA radiative flux	SSF	Terra CERES	20km	instantaneous
Meteorological data	ERA-Interim	ECMWF	0.125°×0.125°	hourly

750 **Table 3: The geographical characteristics, observing period, sample number of sunphotometer sites. The fitted regression equations between MERRA-2 and sunphotometer SSA are also shown here. In the equation, x represents SSA sample, y represents fitted value of SSA.**

Location	Lon/Lat	Observing period	Sample number	Fitted regression equation between MERRA-2 and sunphotometer SSA
Xuzhou (Urban)	117.14°E/34.22°N	2013.8-2016.12	514	y=0.02+0.94x
Shouxian (Rural)	116.78°E/32.56°N	2008.5-2008.12	26	y=-0.45+1.46x
Hefei (Urban)	117.16°E/31.91°N	2005.11-2005.12 2008.1-2008.11	19	y=0.09+0.85x
Taihu (Rural)	120.22°E/31.42°N	2005.1-2012.12 2015.1-2016.12	230	y=0.2+0.75x
Pudong (Urban)	121.79°E/31.05°N	2010.12-2012.10 2014.1-2015.11	84	y=0.49+0.46x
Hangzhou (Urban)	120.16°E/30.29°N	2008.4-2009.2	45	y=0.38+0.57x

755

Table 4: Errors induced by different input parameters in ASY, radiative flux (F_d_sur, F_u_sur) and ADRF. Here, the uncertainties of input parameters (AOD, Albedo, CERES F_u_toa) are from literatures and the uncertainty of SSA is from validation in Section 4.

Parameter	Uncertainty	Errors in ASY	Errors in F_d_sur	Errors in F_u_sur	Errors in ADRF
AOD	±20%[a]	-3.7%~1.7%	~4.5%	~4.4%	~15.4%
SSA	±10%	-19%~23%	~12%	~12%	~24%
Albedo	±5%[b]	-3.7%~1.7%	~0.7%	~5.9%	~3%
CERES F_u_toa	±1.6%[c]	-1.8%~1.7%	~0.4%	~0.4%	~1.5%

[a] He et al. (2010).

760   [b] Cescatti et al. (2012).

[c] Su et al. (2015).

Figure 1: The map of research area, topography, major lakes and mountains in East China. The red circles denotes the locations of three pyranometers (Baoshan, Fuzhou and Yong'an). This figure was generated by ArcGIS, version 10.2. Map source: Map World (National Platform for Common Geospatial Information Services, www.tianditu.gov.cn).

28
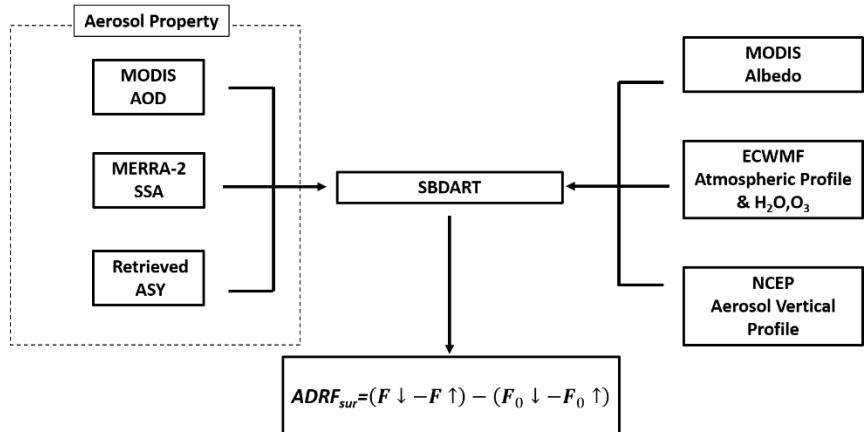
770   **Figure 2: A schematic diagram to simulate ADRF based on satellite and reanalysis datasets.**
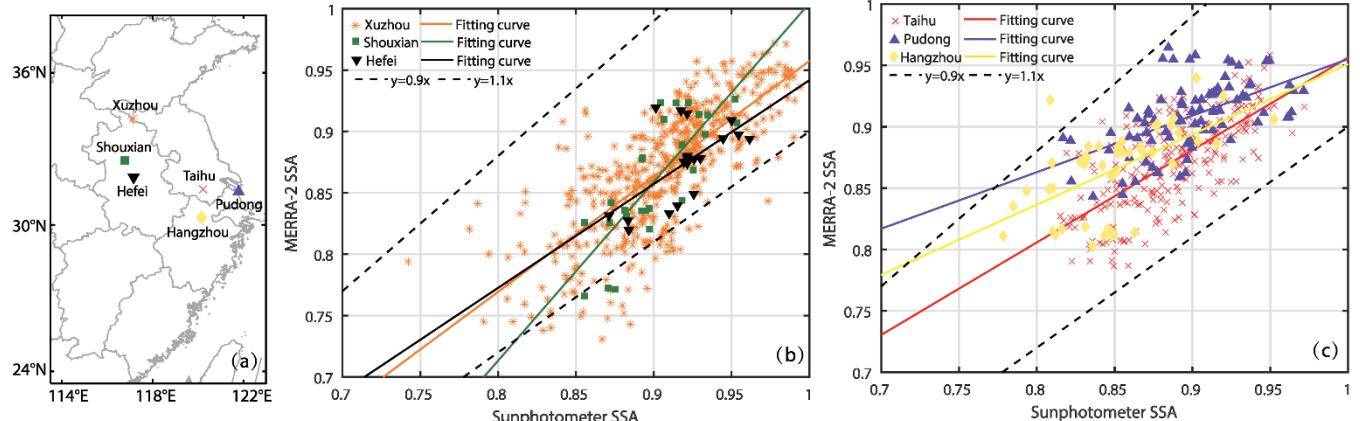
Figure 3: (a) The location of six sunphotometer sites over East China. (b) The scatter plots of SSA between MERRA-2 and sunphotometer in Xuzhou, Shouxian and Hefei. Orange dots represent Xuzhou samples and orange line is the fitting curve of Xuzhou samples while green represents Shouxian and black represents Hefei. Dashed lines are the range of ±10% relative error. (c) The scatter plots of SSA between MERRA-2 and sunphotometer in Taihu, Pudong and Hangzhou. Red dots represent Taihu samples and red line is the fitting curve of Taihu samples while purple represents Pudong and yellow represents Hangzhou. Dashed lines are the range of ±10% relative error.

ASYa(0.1) → F_u_toa_a; ASYb(0.9) → F_u_toa_b

$(F\_u\_toa\_a - F\_u\_toa) \times (F\_u\_toa\_b - F\_u\_toa) < 0$

N → ASY = NaN

Y

$ASYc = \frac{1}{2}(ASYa + ASYb)$
$ASYc → F\_u\_toa\_c$

$|F\_u\_toa\_c - F\_u\_toa| < 1$

Y

N

ASYa = ASYc
F_u_toa _a = F_u_toa_c

N ← $(F\_u\_toa\_a - F\_u\_toa) \times (F\_u\_toa\_c - F\_u\_toa) < 0$ → Y

ASYb = ASYc
F_u_toa _b = F_u_toa_c

ASY = ASYc
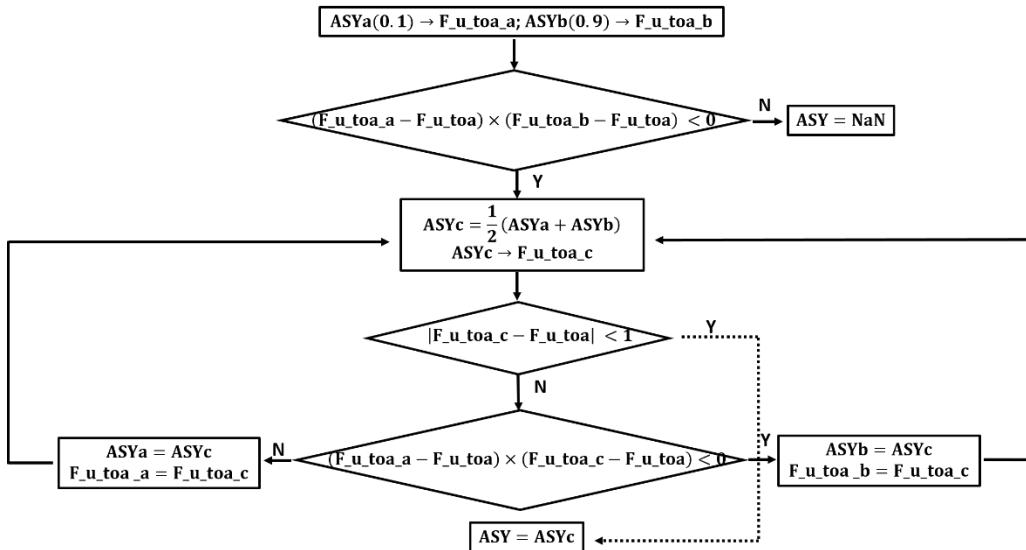
780

Figure 4: A detailed workflow of binary search used in ASY retrieval.

31
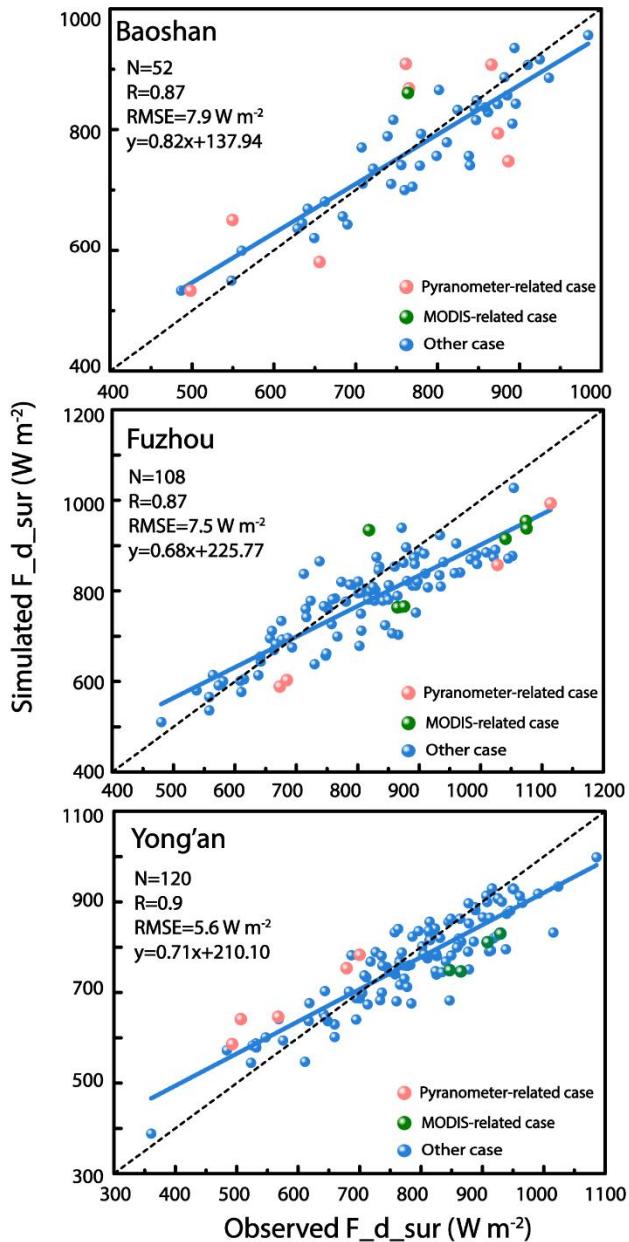
Figure 5: The scatter plots between observed F_d_sur by pyranometers and simulated F_d_sur by SBDART in Baoshan,
Fuzhou, and Yong'an. The blue line the is fitting curve and the dashed line represents y=x. The red dots denote the
specific case in which the pyranometer captures the fluctuation of F_d_sur by clouds during one hour. The olive green
dots denote the specific case in which the site is completely covered by clouds, deduced from MODIS true color map
**composed by 1, 4 and 3 channels. The blue dots represent the other ordinary case.**
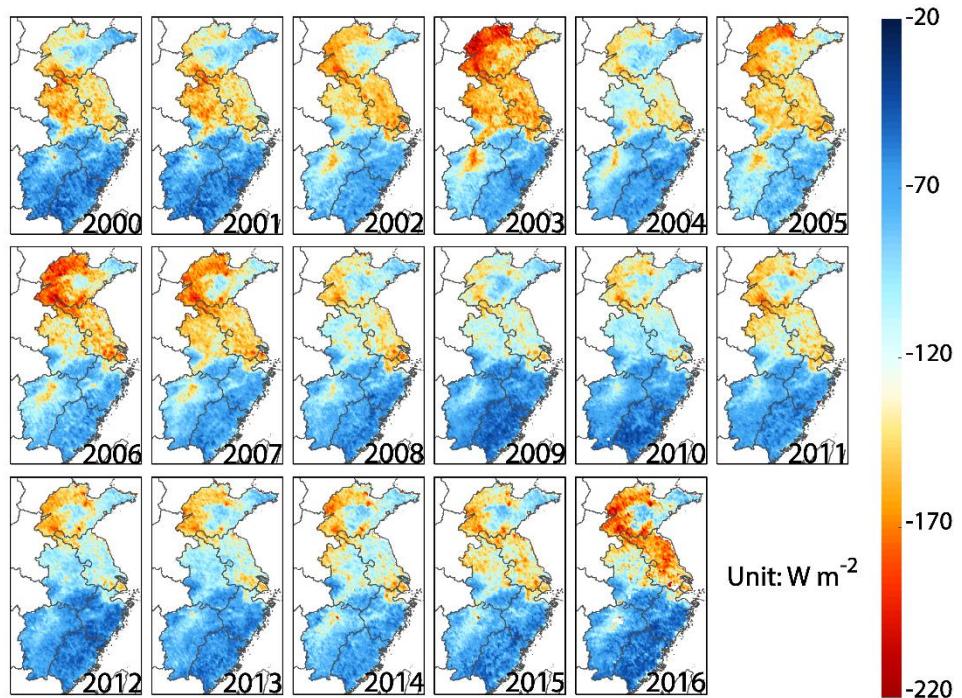
Figure 6: Yearly mean ADRF distributions during 2000-2016 over East China (unit: W m⁻²).
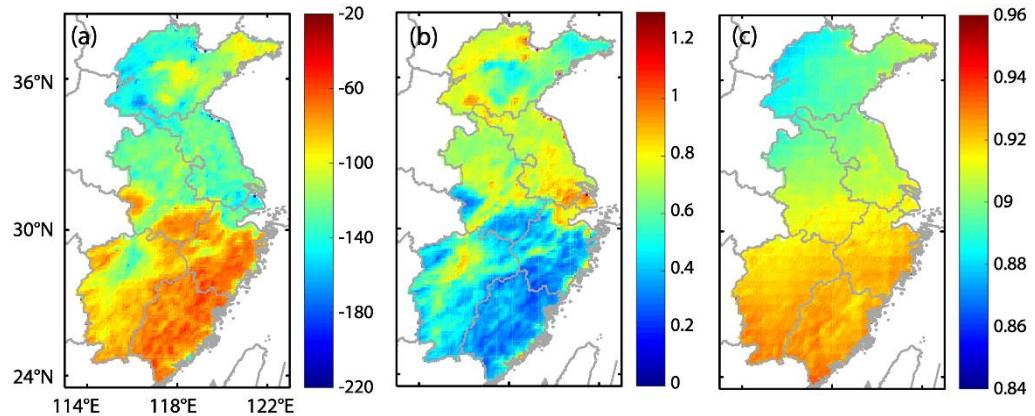
795

Figure 7: Averaged spatial distribution of (a)ADRF (unit: W m⁻²), (b)AOD and (c)SSA during 2000-2016 in the East China.

800
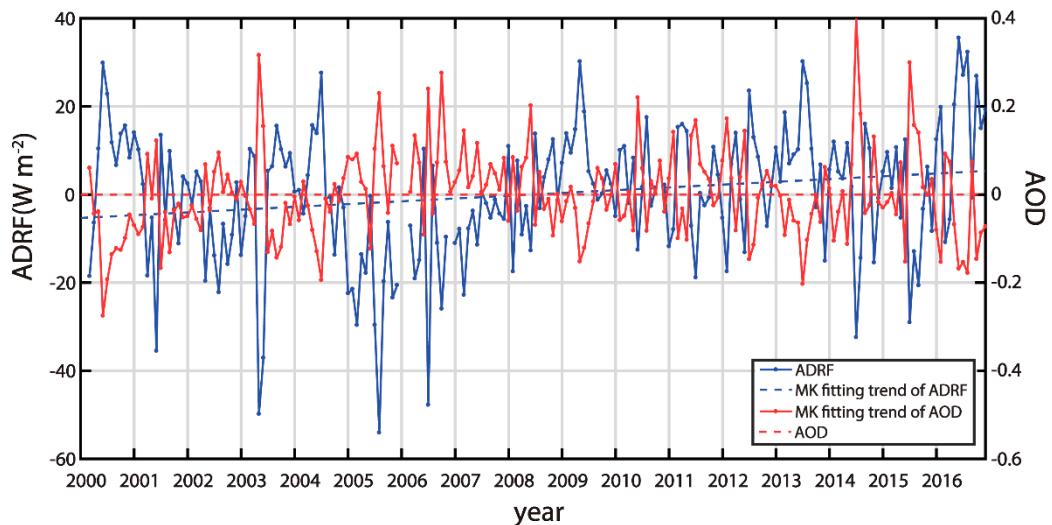
Figure 8: Time series of monthly mean ADRF (blue) and AOD (red) in East China from 2000 to 2016. Dashed lines represent the Mann-Kendell (MK) fitting trend of ADRF and AOD.
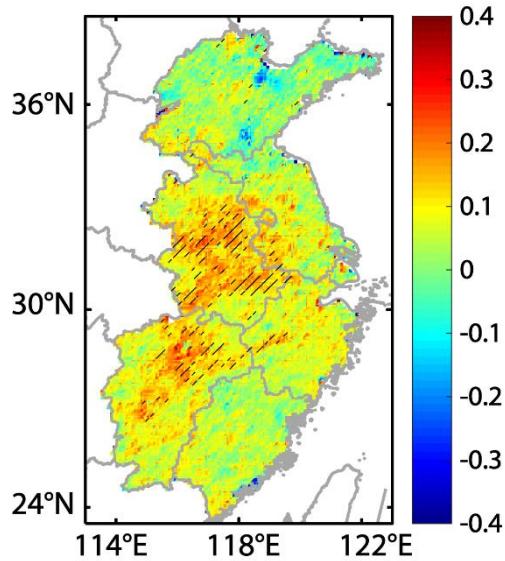
805

Figure 9: The spatial distribution of ADRF trend in East China during 2000-2016 (unit: W m^{-2} month^{-1}). Hatched regions represent those exceeding the 90% significance level.